Monte Carlo modeling of carrier-carrier scattering in semiconductors with nonparabolic bands

Olivier Bonno, Jean-Luc Thobel

Monte Carlo modeling of carrier-carrier scattering in semiconductors with nonparabolic bands

Cite as: J. Appl. Phys. **104**, 053719 (2008); https://doi.org/10.1063/1.2976170
Submitted: 14 May 2008 • Accepted: 03 July 2008 • Published Online: 11 September 2008

Olivier Bonno and Jean-Luc Thobel

Monte Carlo modeling of carrier-carrier scattering in semiconductors with nonparabolic bands

Olivier Bonno[a] and Jean-Luc Thobel
Institut d'Électronique, de Microélectronique et de Nanotechnologie, UMR CNRS 8520, Université des Sciences et Technologies de Lille, Avenue Poincaré, BP 69, 59652 Villeneuve d'Ascq Cédex, France

(Received 14 May 2008; accepted 3 July 2008; published online 11 September 2008)

An efficient algorithm to account for nonparabolicity in carrier-carrier scattering in an ensemble Monte Carlo simulator is proposed. The major difficulty of modeling intercarrier scattering in semiconductors with nonparabolic bands arises from the two particle momentum and energy conservation laws that have to be simultaneously satisfied. A numerically efficient method is thus proposed to compute the final states accounting for a nonparabolic density of states and included in an ensemble Monte Carlo simulator. The developed algorithm makes use of rejection procedures in order to determine the correct number of scattering events as well as the distribution of the final states. This algorithm is then applied to compute constant-energy contours in various semiconductors, including narrow gap, highly nonparabolic materials, such as InAs. The model is also used to investigate the electron dynamics in an InAs quantum well heterostructure. Our results show that nonparabolicity significantly alters the transient regime since it increases the number of carrier-carrier scattering events. Finally, we investigate the validity of the parabolic approximation in the modeling of a typical GaAs resonant phonon terahertz quantum cascade laser. It is shown that, although electron-electron scattering plays a crucial role in setting the device performance of the laser, the effect of nonparabolicity in this interaction alters only slightly the population inversion while the subband temperatures are increased. © *2008 American Institute of Physics*.
[DOI: 10.1063/1.2976170]

I. INTRODUCTION

Carrier-carrier scattering (CCS) has been an important topic in semiconductor physics for decades. In a number of experiments aiming to study excited carrier relaxation,[1–5] it has been shown that mutual Coulomb interaction may be dominant in carrier thermalization, in particular in heterostructures with subband spacings less than the polar optic phonon energy.[5] In a vast array of modern optoelectronic devices, CCS plays a prominent role in the carrier transport. Indeed, electron-electron scattering (EES) has been tremendously investigated in the quantum cascade laser (QCL),[6–11] because this scattering mechanism is essential in setting the performance of QCLs operating in the far-infrared region of the electromagnetic spectrum (1–10 THz). These devices have generated a great deal of interest owing to various possible applications of the terahertz sources, e.g., in chemical sensing, spectroscopy or biomedical imaging. Thus, the understanding of the underlying physical background of CCS is crucial in order to further improve the output characteristics of QCLs, especially in the terahertz range.

Since the early work of Pines and Bohm,[12] the CCS mechanism has been widely investigated in the literature.[13–17] The modeling of this scattering mechanism tackles many issues of both theoretical and numerical natures, particularly in the context of a two-dimensional carrier gas (2DCG). Thus, in order to keep the computational cost reasonable, CCS in many-subband systems such as QCLs is usually modeled in a simplified manner. One of the most frequent hypothesis concerns the band structure. For simplicity it is generally assumed a parabolic dispersion relation. However, the impact of this assumption has not been evaluated. In particular, the influence of nonparabolicity (NP) on the QCL performance has not been studied. In this article, we demonstrate a Monte Carlo simulator, including the CCS mechanism, that is suitable for the study of the transport in semiconductors with nonparabolic bands. Hence, in our model NP is taken into account in the Schrödinger–Poisson solver through the BenDaniel–Duke Hamiltonian[18] as well as in all scattering mechanisms.

The main advantage of assuming parabolic bands when modeling CCS is that energy and momentum conservation equations can be solved analytically,[13] in order to determine the possible final states. On the contrary, in nonparabolic bands this calculation generally requires some kind of brute force method, which dramatically increases the computational cost. In this work, we thus propose an efficient method in order to compute the final states when NP is taken into account, avoiding systematic resolution of the energy and momentum conservation equations in the **K** space. To denote the final states in the **K** space, they will be referred to as "constant-energy contour" or equivalently "equienergy lines" hereafter.

In carrier transport studies, the question of computing the constant-energy contour in nonparabolic bands has only been treated by a few authors,[19–22] and is generally disre-

[a]Present address: CEA/LETI Minatec, 17 rue des Martyrs, 38054 Grenoble, France. Electronic mail: olivier.bonno@laposte.net.

garded as far as weakly nonparabolic semiconductors such as gallium arsenide or silicon are investigated.[7–9,11,13–15,23] This topic has also been tackled by Kane[24] and later by Harrison *et al.*,[25] who calculated impact ionization rates for realistic band structure via Monte Carlo sampling of the multidimensional integral appearing in the expression of the CCS probability. However, the proposed algorithms are either dependent on the screening model[20] or on the dispersion relation,[22] while others require unaffordable computational resources such as Monte Carlo sampling or the Gilat–Raubenheimer method.[26] Moreover, it has been shown in a previous study,[11] that it is necessary to frequently reevaluate the CCS rates during the simulation since the system evolves in nonequilibrium transport conditions. For the study of QCL, a straightforward brute force approach is thus out of the question. Therefore, there is a need for a simplified method that could be used in a Monte Carlo simulator.

To this aim, in this article we describe a Monte Carlo simulator that accounts for NP in the CCS interaction. We propose an efficient numerical method in order to solve the energy and momentum conservation equations entering the CCS rates. The proposed algorithm, which makes no assumption neither on the screening model nor on the nonparabolic dispersion relation, is quite general and may be applied to study carrier-carrier interactions in any quantum wells structure. With this simulator, we study the relaxation of excited carriers in an InAs quantum well heterostructure, i.e., a highly nonparabolic material. Finally, we focus on a state-of-the-art terahertz QCL initially proposed by Williams *et al.*[27] By means of Monte Carlo simulation, we discuss the assumption of parabolic bands in the modeling of this QCL and address the influence of NP on the population inversion as well as internal quantities, such as subband temperatures.

The remainder of this article is organized as follows: In Sec. II, the Monte Carlo algorithm we developed to account for NP in the CCS interaction is described. The main steps of the derivation of the CCS probability are outlined emphasizing the differences between the parabolic and the nonparabolic case. Then, some illustrative examples of the constant-energy contour computation for GaAs, InAs, and Si are presented and discussed. The main results are presented in Sec. III. First, the model is applied to study the relaxation of excited electrons in an InAs heterostructure. Then, the study of a GaAs resonant phonon QCL operating at 3.4 THz is considered. Finally, the main conclusions are summarized in Sec. IV

II. THE MODEL

In Sec. II, we describe the algorithm used to account for NP in the CCS interaction. It is worth mentioning that NP also enters the expression of the EES rates through the polarizability tensor and screening, as it has been shown by Osman and Ferry.[28] In this work, such effects have been disregarded for simplicity.

A. General formulation of the CCS probability in the case of nonparabolic semiconductor bands

The modeling of CCS in the parabolic bands approximation within the framework of a 2DCG has been extensively described in a number of papers.[11,13,15,19,29] Let us recall the basis of the derivation of the scattering probability in order to understand where the assumption of parabolic bands enters the calculation and how it considerably simplifies the scattering rate expression. Hence, the method to handle nonparabolic bands would be easier to understand. We consider a principal carrier in state $|\lambda\mathbf{K}\rangle$ that scatters with a partner carrier in subband μ with wave vector $\mathbf{P}$. The final states are denoted $|\lambda'\mathbf{K}'\rangle$ and $|\mu'\mathbf{P}'\rangle$, respectively. Using the Fermi golden rule, the probability $s_{\lambda\lambda'}(\mathbf{K})$ for a transition from $|\lambda\mathbf{K}\rangle$ to $|\lambda'\mathbf{K}'\rangle$, via a Coulomb interaction, is[15]

$$s_{\lambda\lambda'}(\mathbf{K}) = \frac{2\pi}{\hbar}\frac{1}{\mathcal{A}^2}\sum_{\mu\mu'\mathbf{P}\mathbf{P}'} f_\mu(\mathbf{P})|M_{\lambda\mu\lambda'\mu'}(\mathbf{Q})|^2\delta[E_{\lambda'}(\mathbf{K}') + E_{\mu'}(\mathbf{P}') - E_\lambda(\mathbf{K}) - E_\mu(\mathbf{P})], \quad (1)$$

where $\mathcal{A}$ is the normalization area, $f_\mu(\mathbf{P})$ is the distribution function for a state $|\mu\mathbf{P}\rangle$, and $E_\mu(\mathbf{P})$ is the total energy of that state, $\mathbf{Q}=\mathbf{K}-\mathbf{K}'$ is the exchanged wave vector and $M_{\lambda\mu\lambda'\mu'}(\mathbf{Q})$ is the matrix element of the transition. To obtain this equation, one has used the conservation of the parallel momentum to simplify the summation over $\mathbf{K}'$.[30] This writes

$$\mathbf{T} \equiv \mathbf{K} + \mathbf{P} = \mathbf{K}' + \mathbf{P}'. \quad (2)$$

Thus, as it can be seen from the argument of the δ-function in Eq. (1), one of the main difficulties of handling NP arises from the fact that, owing to momentum conservation, $\mathbf{P}'$ not only enters the expression of $E_{\mu'}(\mathbf{P}')$ but also that of $E_{\lambda'}(\mathbf{K}')=E_{\lambda'}(\mathbf{T}-\mathbf{P}')$.

We rewrite Eq. (1) in the following form:

$$s_{\lambda\lambda'}(\mathbf{K}) = \frac{1}{2\pi\hbar\mathcal{A}}\sum_{\mu\mu'\mathbf{P}} f_\mu(\mathbf{P})\mathcal{E}_{\lambda\mu\lambda'\mu'}(\mathbf{K},\mathbf{P}), \quad (3)$$

with

$$\mathcal{E}_{\lambda\mu\lambda'\mu'}(\mathbf{K},\mathbf{P}) = \int\int \left|M_{\lambda\mu\lambda'\mu'}\left(\mathbf{W}-\frac{\mathbf{G}}{2}\right)\right|^2 \times \delta[E^{\text{fin}}_{\lambda'\mu'}(\mathbf{W},\mathbf{T}) - E^{\text{ini}}_{\lambda\mu}(\mathbf{K},\mathbf{P})]d^2\mathbf{W}, \quad (4)$$

where $\mathbf{G}\equiv\mathbf{P}-\mathbf{K}$. To obtain Eq. (4), one makes use of the substitution $\mathbf{W}=\mathbf{P}'-\mathbf{T}/2$. The terms $E^{\text{ini}}_{\lambda\mu}$ and $E^{\text{fin}}_{\lambda'\mu'}$ in the energy-conserving δ-function have the following expressions:

$$E^{\text{ini}}_{\lambda\mu}(\mathbf{K},\mathbf{P}) = \varepsilon_\lambda(\mathbf{K}) + \varepsilon_\mu(\mathbf{P}) + e_\lambda + e_\mu,$$

$$E^{\text{fin}}_{\lambda'\mu'}(\mathbf{W},\mathbf{T}) = \varepsilon_{\lambda'}\left(\frac{\mathbf{T}}{2}-\mathbf{W}\right) + \varepsilon_{\mu'}\left(\frac{\mathbf{T}}{2}+\mathbf{W}\right) + e_{\lambda'} + e_{\mu'}, \quad (5)$$

where e_λ is the eigenenergy associated with the λth state and $\varepsilon_\lambda(\mathbf{K})$ is the kinetic part of the total energy $E_\lambda(\mathbf{K})$.

1. Parabolic bands

At this step of the calculation, we now assume a simple parabolic dispersion relation of the form

$$\varepsilon_\lambda(\mathbf{K}) = \frac{\hbar^2\mathbf{K}^2}{2m^*}, \tag{6}$$

where m^* is the carrier effective mass. In this case, the energy-conserving δ-function writes

$$\delta[E^{\text{fin}}_{\lambda'\mu'}(\mathbf{W},\mathbf{T}) - E^{\text{ini}}_{\lambda\mu}(\mathbf{K},\mathbf{P})] = \frac{m^*}{\hbar^2}\delta\left[\left(\mathbf{P}' - \frac{\mathbf{T}}{2}\right)^2 - \mathcal{R}^2_{\lambda\mu\lambda'\mu'}\right]$$
$$= \frac{m^*}{\hbar^2}\delta(\mathbf{W}^2 - \mathcal{R}^2_{\lambda\mu\lambda'\mu'}), \tag{7}$$

$\mathcal{R}_{\lambda\mu\lambda'\mu'}$ having the following expression:

$$\mathcal{R}_{\lambda\mu\lambda'\mu'} = \frac{1}{2}\left[\frac{4m^*}{\hbar^2}(e_\lambda + e_\mu - e_{\lambda'} - e_{\mu'}) + G^2\right]^{1/2},$$
$$= \frac{1}{2}[\Delta e_{\lambda\mu\lambda'\mu'} + G^2]^{1/2}. \tag{8}$$

Using the energy-conserving δ-function [Eq. (7)], the summation over $\mathbf{W}$ can be simplified to obtain the CCS probability in the parabolic approximation used in our previous works,[11,29,31]

$$s^{\text{parab}}_{\lambda\lambda'}(\mathbf{K}) = \frac{m^*}{4\pi\hbar^3\mathcal{A}}\sum_{\mu\mu'\mathbf{P}} f_\mu(\mathbf{P})\int_0^{2\pi}|M_{\lambda\mu\lambda'\mu'}(Q)|^2 d\beta, \tag{9}$$

where β is the angle between $\mathbf{W}$ and $\mathbf{G}$ and the superscript "parab" stands for parabolic bands. The magnitude of the wave vector $\mathbf{W}$ is given by Eq. (7), i.e., $W=\mathcal{R}_{\lambda\mu\lambda'\mu'}$. Hence, as $\mathbf{Q}=\mathbf{W}-\mathbf{G}/2$, the usual conservation law used by many authors in their Monte Carlo simulators is easily recovered, namely,

$$Q = \frac{1}{2}[2G^2 + \Delta e_{\lambda\mu\lambda'\mu'} - 2G(\Delta e_{\lambda\mu\lambda'\mu'} + G^2)^{1/2}\cos\beta]^{1/2}.$$

2. Nonparabolic bands

Henceforth, we consider the general case of nonparabolic bands that we should mark through the superscript "np" thereafter. In that case, $\mathcal{E}^{\text{np}}_{\lambda\mu\lambda'\mu'}(\mathbf{K},\mathbf{P})$ cannot be simplified as for parabolic bands. In particular, it is no longer possible to factorize the energy-conserving δ-function as in Eq. (7). Thus, the calculation of the final energies that satisfy the energy conservation law has to be performed numerically. Indeed, one has to evaluate the following sum over polar angle:

$$\mathcal{E}^{\text{np}}_{\lambda\mu\lambda'\mu'}(\mathbf{K},\mathbf{P}) = \int_0^{2\pi} W_0\left|M_{\lambda\mu\lambda'\mu'}\left(\mathbf{W}_0 - \frac{\mathbf{G}}{2}\right)\right|^2\Omega(\mathbf{W}_0)d\beta, \tag{10}$$

where

$$\Omega(\mathbf{W}_0) = \left|\frac{dE^{\text{fin}}_{\lambda'\mu'}(\mathbf{W},\mathbf{T},\beta)}{dW}\right|^{-1}_{\mathbf{W}=\mathbf{W}_0}. \tag{11}$$

The notation $\mathbf{W}_0(\beta)$ stands for the solution for a given value of the polar angle β of $E^{\text{fin}}_{\lambda'\mu'}[\mathbf{W}(\beta),\mathbf{T}]-E^{\text{ini}}_{\lambda\mu}(\mathbf{K},\mathbf{P})=0$, an equation that we write $\Delta E_\beta(\mathbf{W})=0$ hereafter for brevity. In Eq. (10), the term $\Omega(\mathbf{W}_0)$ can be interpreted in terms of density of states. As it can be noticed, the critical point is the determination of $\mathbf{W}_0(\beta)$, which is performed during the Monte Carlo simulation. Before going even further, let us now describe in details this algorithm.

B. The Monte Carlo algorithm

In Monte Carlo simulation, CCS is generally treated via a rejection technique in order to account for the really observed partner distribution function $f_\mu(\mathbf{P})$.[11,13] This approach requires an upper bound of $s_{\lambda\lambda'}(\mathbf{K})$ and therefore one needs to maximize $\mathcal{E}_{\lambda\mu\lambda'\mu'}(\mathbf{K},\mathbf{P})$ irrespective of the unknown partner state $|\mu\mathbf{P}\rangle$. However, as no obvious upper bound of Eq. (10) can be found, we propose to take a multiple of the upper bound used in the parabolic approximation,[19] so we suppose that

$$\mathcal{E}^{\text{np}}_{\lambda\mu\lambda'\mu'} < \Lambda \times \mathcal{E}^{\text{parab}}_{\lambda\mu\lambda'\mu'},$$
$$< \frac{\Lambda m^*\pi}{\hbar^2}\mathcal{M}^2_{\lambda\mu\lambda'\mu'}, \tag{12}$$

where Λ is an adequate multiple and $\mathcal{M}^2_{\lambda\mu\lambda'\mu'}$ is the maximum value of the transition matrix element accounting for exchange scattering, i.e.,

$$|M_{\lambda\mu\lambda'\mu'}(Q)|^2 = \frac{1}{2}[|V_{\lambda\mu\lambda'\mu'}(Q)|^2 + |V_{\lambda\mu\mu'\lambda'}(Q')|^2$$
$$- V_{\lambda\mu\lambda'\mu'}(Q)V_{\lambda\mu\mu'\lambda'}(Q')], \tag{13}$$

where $\mathbf{Q}'=\mathbf{K}-\mathbf{P}'$ and $V_{\lambda\mu\lambda'\mu'}(Q)$ is the screened Coulomb potential matrix element. Hence, the following upper bound of $s^{\text{np}}_{\lambda\lambda'}(\mathbf{K})$ is used during the simulation,

$$S^{\text{np}}_{\lambda\lambda'} = \frac{\Lambda m^*}{2\hbar^3}\sum_{\mu\mu'} n_\mu\mathcal{M}^2_{\lambda\mu\lambda'\mu'}, \tag{14}$$

where n_μ is the charge density of subband μ. As in our previous work,[11] only one-half on this quantity is employed in order to avoid double counting of the probability.[15,32]

During the simulation, once a CCS event has been chosen according to the upper bound $S^{\text{np}}_{\lambda\lambda'}$, the algorithm proceeds in the following manner. First, the partner electron $|\mu\mathbf{P}\rangle$ is randomly selected from the ensemble. Then, for each subband μ', the quantity $\mathcal{E}^{\text{np}}_{\lambda\mu\lambda'\mu'}(\mathbf{K},\mathbf{P})$ is numerically evaluated over a mesh of polar angle β. The detailed method to compute $\mathbf{W}_0(\beta)$ is explained hereafter in Sec. II C. Note that this step of the calculation is very time consuming because all subbands μ' are explored. Then, a rejection technique is employed in order to take the distribution function really encountered during the simulation into account. This is the

counterpart of the maximization performed in Eq. (12). Therefore, selecting a random number r uniformly between 0 and 1, the following inequality is tested:

$$r \times \frac{\Lambda m^* \pi}{\hbar^2} \sum_{\mu'} \mathcal{M}^2_{\lambda\mu\lambda'\mu'} < \sum_{\mu'} \mathcal{E}^{\mathrm{np}}_{\lambda\mu\lambda'\mu'}(\mathbf{K},\mathbf{P}). \quad (15)$$

If Eq. (15) is fulfilled, the number r is also used to determine the final subband μ' of the partner electron as well as the wave vector $\mathbf{W}_0$ according to the integrand of Eq. (10). Thanks to $\mathbf{W}_0$ and $\mathbf{T}$, the final wave vectors $\mathbf{K}'$, $\mathbf{P}'$ are also computed. Then the Pauli principle is accounted for to complete the treatment of the CCS event. Note that if Eq. (15) is not satisfied, the collision is rejected and the so-called "self-scattering event" occurs.[13]

C. Determination of the constant-energy contour: Resolution of $\Delta E_\beta(\mathbf{W})=0$

In Sec. II C, we describe the numerical method used to compute the wave vector $\mathbf{W}_0$ satisfying $\Delta E_\beta(\mathbf{W})=0$. Fischetti and Laux[19,22] have performed such a calculation. For example, Fischetti and Laux[22] have solved $\Delta E_\beta(\mathbf{W})=0$ using standard methods for quartic algebraic equation within the Kane approximation, i.e., using $\hbar^2K^2/2m^*=\varepsilon(1+\alpha\varepsilon)$, where α is the NP coefficient. However, this method depends on the dispersion relation and cannot be used in the case of warped bands or numerically computed bands, e.g., those obtained by the $\mathbf{k}\cdot\mathbf{p}$ method. A systematic exploration of the $\mathbf{K}$ space can also be adopted. However, such a method that has to be performed for each values of β and μ' is prohibitive, especially in many-subband systems such as QCLs.

We are thus seeking a method that has the following features: (i) it could be applied to any kind of nonparabolic dispersion relation, thus to electrons as well as to holes; (ii) the computational cost has to be reasonable. Therefore, an iterative algorithm has been developed using the fact that the value of $\mathbf{W}_0$ in the nonparabolic case is a correction of the parabolic one. However, in this case, it is readily noticed in Eq. (7) that the constant-energy contour is a circle of radius $\mathcal{R}_{\lambda\mu\lambda'\mu'}$ centered at $\mathbf{T}/2$. This contour would be referred to as the "parabolic circle" in the following discussion: To obtain the contour corrected by NP, a bisection method is used to compute, for each fixed value of the angle β, the magnitude of the wave vector $\mathbf{W}_0(\beta)$ that satisfies the energy-conserving δ-function. In practice, the bounds of the starting research interval are chosen as multiples of $\mathcal{R}_{\lambda\mu\lambda'\mu'}$, e.g., $2^{\pm\xi}\mathcal{R}_{\lambda\mu\lambda'\mu'}$. Note that, when it is already clear that energy conservation would be impossible, intermediate tests greatly speed up the calculation by bypassing later computations.

Before presenting the calculation of equienergy lines in various materials, we would like to make some technical remarks. Equation $\Delta E_\beta(\mathbf{W})=0$ is solved exactly for the whole range $[0,2\pi]$ of the polar angle β, although this task can be much reduced using symmetry. In practice, good tradeoffs between computational speed and accuracy are obtained using $\xi=2$. For the value of Λ, we distinguish InAs and GaAs: Λ has been taken to 10 and 4, respectively. Moreover, if the parameter Λ used to compute the scattering rate upper bound becomes too small during the simulation, a new one is used (in practice $\Lambda \rightarrow 2^p\Lambda$) in order to self-consistently account for the redistribution of the carriers.

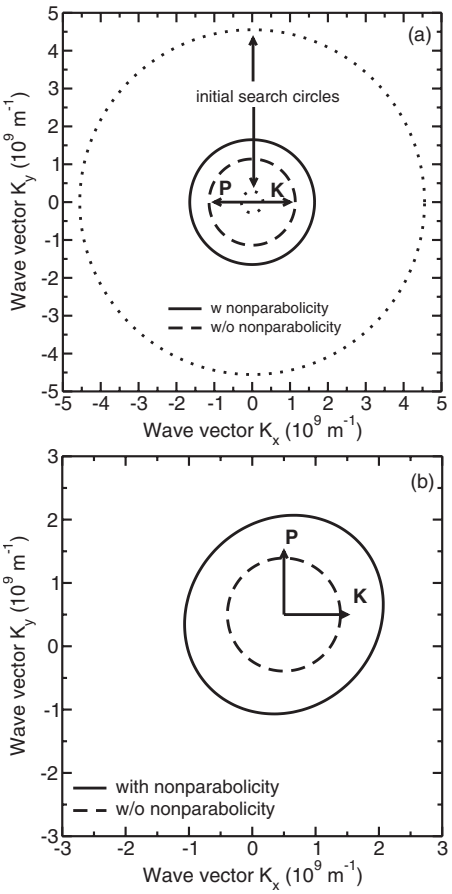

FIG. 1. Equienergy lines, i.e., the calculated wave vectors $\mathbf{P}'$ solutions of $\Delta E_\beta(\mathbf{P}'-\mathbf{T}/2)=0$, with (solid line) and without (dashed line) accounting for the NP in the dispersion relation. The transition considered is M_{2211}. The structure consists in an InAs infinite square-quantum well of width 100 Å. The following two cases were considered: (a) $\mathbf{K}=-\mathbf{P}$; (b) $\mathbf{K}\cdot\mathbf{P}=0$. For both examples, we have taken $K_x=10^9$ m^{-1} and $K_y=0$. For clarity, the vectors $\mathbf{K}$ and $\mathbf{P}$ are sketched on the figure. In the top panel, we also draw the circles used as the initial guess interval for the computation, i.e., $2^{\pm\xi}\mathcal{R}_{2211}$ with $\xi=2$.

D. Equienergy lines in InAs, GaAs, and Si

It is useful to illustrate in some detail the equienergy lines in a few cases of interest. As a first example, we consider an infinite InAs square-quantum well of width $L=100$ Å. InAs is a narrow gap material; thus its NP coefficient is large: using the well known $\mathbf{k}\cdot\mathbf{p}$ formula,[33] one has $\alpha\approx(1-m^*/m_0)^2/E_g$, where m_0 is the free electron mass and E_g the gap energy. With $m^*=0.023m_0$ and $E_g=0.354$ eV,[34] α_{InAs} is taken as 2.7 eV^{-1}. In this example, as well as in the remainder of this paper when electrons are studied, we used the nonparabolic dispersion relation presented by Thobel *et al.*[18]

Figure 1 shows the constant-energy contours, i.e., the ensemble of wave vectors $\mathbf{P}'$ satisfying $\Delta E_\beta(\mathbf{P}'-\mathbf{T}/2)=0$ for the transition M_{2211} with (solid line) and without (dashed line) accounting for NP in the dispersion relation. As illustrative examples, we have chosen two different values of the

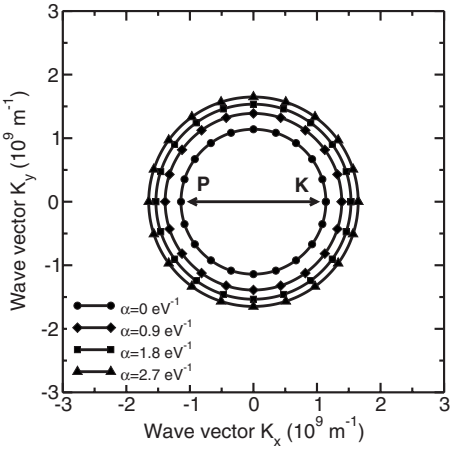

FIG. 2. Equienergy lines for the M_{2211} transition for various values of the NP coefficient: (●) $\alpha=0$ eV^{-1}; (♦) $\alpha=0.9$ eV^{-1}; (■) $\alpha=1.8$ eV^{-1}; and (▲) $\alpha=2.7$ eV^{-1}. The same structure as well as the same parameters as in Fig. 1 were used.

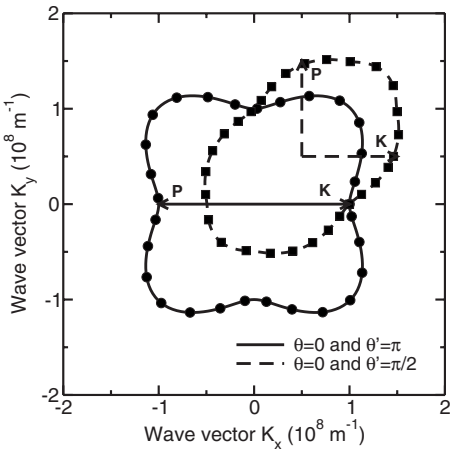

FIG. 3. Equienergy lines for the M_{1111} transition for the case of HH in a $Si_{0.75}Ge_{0.25}$ infinite square-quantum well of width 100 Å. The following two values of the polar angle θ' of wave vector **P** are considered: $\theta'=\pi$ (solid line) and $\theta'=\pi/2$ (dashed line). For both cases, K_x is set to 10^8 m^{-1}; the polar angle is set θ to 0. The wave vectors **K** and **P** are also sketched on the figure. The closed symbols represent the equienergy lines obtained using a systematic exploration of the **K** space in order to solve the energy conservation equation.

initial wave vectors **K** and **P**, thus giving two values for **T** and **G**, the two parameters describing the parabolic circle. First, the case $\mathbf{K}=-\mathbf{P}$ has been considered [Fig. 1(a)] and then the example $\mathbf{K}\cdot\mathbf{P}=0$ has been examined [Fig. 1(b)]. We note (K_x,K_y) and $(K\cos\theta, K\sin\theta)$ the Cartesian and polar coordinates of the wave vector **K**, respectively. For both cases, **K** has only a x-axis component, set to 10^9 m^{-1}. In Fig. 1(a), we have also plotted the two circles $(2^{\pm\xi}\mathcal{R}_{2211},\xi=2)$ used to start the bisection computation. One can see in Figs. 1(a) and 1(b) that when NP is taken into account, higher values of P' are obtained, of the order of 40% greater than those calculated in the case of parabolic bands.

When NP is negligible, i.e., when α is small or almost null, one should recover the equienergy line of the parabolic band case, i.e., as we have previously shown, the parabolic circle. To check the behavior of our method, we have *artificially* modified the NP coefficient α starting from 2.7 down to 0 eV^{-1} by a step of 0.9 eV^{-1}. In Fig. 2, the resulting computed equienergy lines with a varying α for the structure of Fig. 1 are plotted. One can notice that, as expected, the parabolic circle [dashed line in Fig. 1(a) or curve with filled circles in Fig. 2] is recovered when $\alpha\to 0$, i.e., as the limiting case of a null NP coefficient. This supports the correctness of our method.

Even though in this article we have applied the Monte Carlo only to electrons in the conduction band of III-V semiconductors, we stress that it could be used in more general circumstances. Therefore, as another test bed, we have applied our method to compute equienergy lines of holes in Si. In such a material, the light (LH) and heavy (HH) holes dispersion relations are warped. In a first approximation, the energy equation can be expressed as[33,35]

$$\varepsilon_{\mathrm{LH/HH}}(\mathbf{K})=\frac{\hbar^2K^2}{2m_0}[\gamma_1\pm\mathcal{G}(\mathbf{K})], \tag{16a}$$

with

$$\mathcal{G}(\mathbf{K})=\left[4\gamma_2^2+\frac{12(\gamma_3^2-\gamma_2^2)}{K^4}K_x^2K_y^2\right]^{1/2},$$
$$=[4\gamma_2^2+12(\gamma_3^2-\gamma_2^2)\cos^2\theta\sin^2\theta]^{1/2}, \tag{16b}$$

where γ_1, γ_2, and γ_3 are the Luttinger parameters and the + and − signs refer to LH and HH bands, respectively. To account for the NP in the valence bands, we have used Kane's model.[36] Therefore, the nonspherical, nonparabolic valence band dispersion relations have the form $\hbar^2K^2/(2m_0)=\chi_j(\varepsilon,\theta)$, where the functions $\chi_j(\varepsilon,\theta)$ are the roots of a cubic equation $H_3(\varepsilon,\theta)\chi^3+H_2(\varepsilon,\theta)\chi^2+H_1(\varepsilon)\chi+H_0(\varepsilon)=0$. The index j runs over the three holes bands, i.e., $j=$HH,LH or split off (see Refs. 36 and 37 for further details).

In Fig. 3, we have plotted the equienergy lines of a M_{1111} transition for the case of HH. The structure consists in an infinite $Si_{0.75}Ge_{0.25}$ square-quantum well with $L=100$ Å. The same conditions as in Fig. 1 were used, i.e., only a K_x component for **K** and the following two cases: (i) $\mathbf{K}-\mathbf{P}=0$ (solid line) and (ii) $\mathbf{K}\cdot\mathbf{P}=0$ (dashed line). For this example, K_x was set to 10^8 m^{-1}. In these cases, little influence of the NP is found and Eqs. (16a) and (16b) can be used instead of the full computation of Kane's cubic equation roots. To compute the equienergy lines we have linearly interpolated the Luttinger γ coefficients between those of Si and Ge. For the purpose of illustration, we have also superimposed the equienergy lines obtained using a systematic exploration of the **K** space (closed symbols on Fig. 3), i.e., searching for doublets (P_x',P_y') that satisfy $|E_1(\mathbf{K})+E_1(\mathbf{P})-E_1(P_x',P_y')-E_1(T_x-P_x',T_y-P_y')|=0$ with a given accuracy. We thus verify on Fig. 3 that for both cases (i) and (ii) the results obtained with our method are in good agreement with those of the **K** space exploration. This confirms that our method can also be applied to study valence bands with a reduced computational cost.

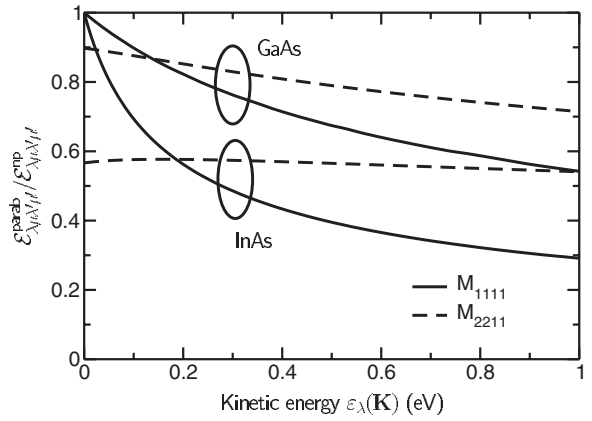

FIG. 4. Calculated ratio $\mathcal{E}^{parab}_{\lambda\mu\lambda'\mu'}/\mathcal{E}^{np}_{\lambda\mu\lambda'\mu'}$ [see Eq. (10) in the text for definition] as a function of the initial kinetic energy $\varepsilon_\lambda(\mathbf{K})$ for GaAs and InAs infinite square-quantum wells of width 100 Å. Solid line: the transition M_{1111}. Dashed line: the transition M_{2211}.

E. Density of states

We now discuss the influence of the nonparabolic density of states $\Omega(\mathbf{W})$. To this aim, we have plotted in Fig. 4 the ratio $w_{\lambda\mu\lambda'\mu'}=\mathcal{E}^{parab}_{\lambda\mu\lambda'\mu'}/\mathcal{E}^{np}_{\lambda\mu\lambda'\mu'}$ as a function of the kinetic energy $\varepsilon_\lambda(\mathbf{K})$ for the following two materials: GaAs and InAs, i.e., a low ($\alpha_{GaAs}=0.6$ eV^{-1}) and high ($\alpha_{InAs}=2.7$ eV^{-1}) nonparabolic one. Moreover, the following two kinds of transitions are considered: a so-called "pure intrasubband" transition, M_{1111}, and the transition M_{2211}. As in previous examples, a 100 Å infinite square well has been considered. For this study, the initial energies $\varepsilon_\lambda(\mathbf{K})$ and $\varepsilon_\mu(\mathbf{P})$ are taken as equal. Other calculation parameters are as follows: screening by only the ground subband, with a polarizability factor Π_{11} of 10^8 m^{-1}, no exchange scattering and electron form factors set to unity for simplicity [they are needed to compute $M_{\lambda\mu\lambda'\mu'}$, see, e.g., Eq. (6) of Ref. 11]. More details about the expression of $\Omega(\mathbf{W}_0)$ entering in Eq. (10) are given in the Appendix. One can observe that, for GaAs, w_{1111} as well as w_{2211} are slightly lower than unity, confirming little influence of NP. For InAs, the influence of NP is, as expected, higher: w_{1111} reaches 60% for about $\varepsilon=0.2$ eV for example. The higher $\mathcal{E}^{np}_{\lambda\mu\lambda'\mu'}$, the higher the EES probabilities in the Monte Carlo simulator. Moreover, for both materials w_{2211} is almost constant, reaching a smaller value in InAs due to a higher NP coefficient. Note that, thanks to these results, one can have a more precise idea of the value of Λ that should be used in the Monte Carlo simulator (see values given at the end of Sec. II C).

In this section, we have presented an algorithm that accounts for NP in the CCS interaction. This numerical method was used to set up a Monte Carlo simulator.

III. MONTE CARLO RESULTS

We now present the results of our Monte Carlo simulation. Other features of the model are standard and have been extensively described in previous papers.[11,18,38] Let us recall them briefly here: (i) The electron states are calculated within the framework of envelope function theory accounting for a nonparabolic BenDaniel–Duke Hamiltonian.[18] (ii)

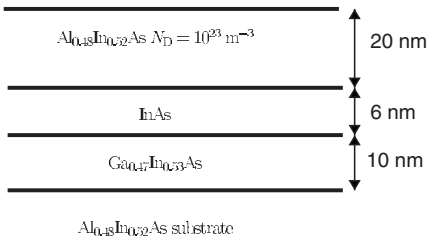

FIG. 5. Sketch of the simulated $Al_{0.48}In_{0.52}As/InAs/Ga_{0.47}In_{0.53}As/Al_{0.48}In_{0.52}As$ heterostructure.

The main scattering mechanisms are included in the simulation, namely, phonon (both polar optic and acoustic), ionized impurity, and alloy scattering. (iii) The model accounts for the Bloch overlap factor for all scattering mechanisms by means of a rejection technique described by Thobel *et al.*[18] (iv) Finally, the Pauli principle is accounted for using the approach developed by Borowik and Thobel *et al.*[39]

A. Relaxation of excited carriers in an InAs quantum well

To study the influence of NP on the electron dynamics, we have applied our model to an InAs quantum well. Although such a heterostructure has not been previously examined before—neither theoretically nor experimentally—we think that it can be interesting to compare the results obtained with and without NP in the CCS interaction in the case of a highly nonparabolic material such as InAs. Thus, as a typical example, we have studied the relaxation of excited electrons in the heterostructure sketched in Fig. 5. The structure consists in an InAs quantum well with width of 6 nm sandwiched between an upper $Al_{0.48}In_{0.52}As$ barrier of thickness 20 nm and a $Ga_{0.47}In_{0.53}As$ layer that is 10 nm thick. The substrate consists in an $Al_{0.48}In_{0.52}As$ thick buffer. Although the misfit between the lattice constant of InAs and $Ga_{0.47}In_{0.53}As$ is pronounced (~3%), we assume no stress in the InAs layer as its thickness is 6 nm, thus below the critical thickness. All layers are unintentionally doped, with a density of residual impurities of 10^{21} m^{-3} except the upper $Al_{0.48}In_{0.52}As$ barrier whose doping level is $N_D=10^{23}$ m^{-3}.

As initial conditions, all carriers are placed in the third subband according to a "heated" Gaussian energy distribution function of mean $\overline{\varepsilon_3}=0.5$ eV and standard deviation $\sigma_3=50$ meV in order to model the shape of the energy distribution obtained after a laser pulse.[14,40,41] The band profile as well as the first five subbands of the structure of Fig. 5 are shown in Fig. 6 at a lattice temperature of 200 K and an electron density N_s of 2×10^{16} m^{-2}. We monitor 10^4 particles during 30 ps using a constant time step of 0.5 fs. Every 10 time steps the electron-electron upper bounds are reevaluated. To compute the constant-energy contour, the range of the polar angle β is divided into 50 intervals of equal width.

We now present the results of the Monte Carlo simulation of the structure of Fig. 6. First, in order to discuss the influence of NP, Fig. 7 represents the time evolution of the fractional subband densities with and without taking into account NP in the EES modeling. One notices a significant influence on the transient regime. In particular, the population of subband 3 decays more rapidly when NP is taken into

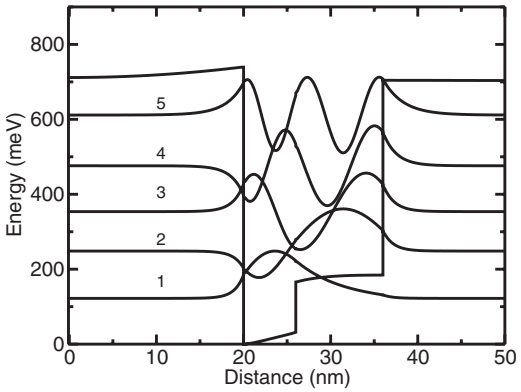

FIG. 6. Conduction band profile and first five wave functions of the heterostructure of Fig. 5 obtained by a self-consistent resolution of Schrödinger and Poisson equations. The total electron density is $N_s=2\times10^{16}$ m^{-2} at 200 K. The wave functions have been shifted in energy so that their respective zero corresponds to the quantized energy level.

account. This a direct consequence of the increased number of Coulomb scattering events. The average scattering times τ_{ij}, calculated by counting the transitions between subbands i and j, are reported in Table I. We notice that electron-electron is the dominant scattering mechanism, especially for intersubband transitions. Its probability is increased, by typically a factor of 2 when NP is accounted for and as a result the system relaxes faster. For example the population of subband 3 decays more rapidly whereas that of subband 1 grows up faster. The effect on the population of subband 2 seems less pronounced because the numbers of $3\rightarrow2$ and $2\rightarrow1$ processes are increased by a similar amount.

B. GaAs/Al$_x$Ga$_{1-x}$As resonant phonon QCL

A lot of previous theoretical studies of QCLs have included the effect of CCS.[7–11,23,42–46] However, to our knowledge, none of them has accounted for NP everywhere in the simulation (i.e., both in the Schrödinger–Poisson solver and in the scattering model). In Sec. III B, we present some results of Monte Carlo simulation of a terahertz QCL, paying special attention to the investigation of the validity of the parabolic approximation. The considered structure is the well-known resonant phonon QCL designed by Williams *et al.*[27] operating at 3.4 THz. The conduction-band profile and

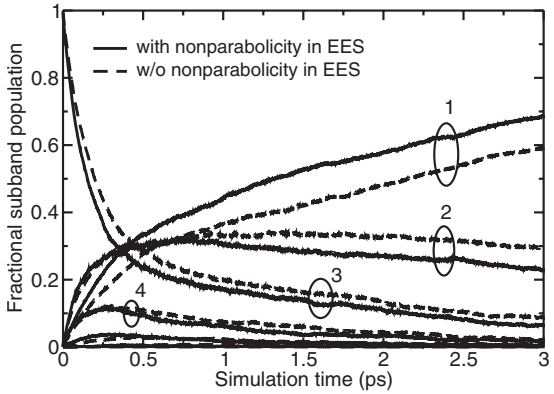

FIG. 7. Fractional subband occupations at 200 K vs simulation time with (solid line) and without (dashed line) accounting for the NP in the CCS interaction. The simulated structure is that in Fig. 6.

TABLE I. Scattering times, in picoseconds, for the main scattering processes from subband i to subband j. First column: polar optic scattering. Second column: EES when NP is accounted for (our model). Third column: EES when NP is neglected.

$i\rightarrow j$	τ_{ph}	τ_{ee}^{NP}	τ_{ee}^{Parab}
$1\rightarrow1$	0.3	0.085	0.19
$1\rightarrow2$	7	0.75	1.34
$1\rightarrow3$	14	1.45	2.6
$2\rightarrow1$	1.9	0.44	1.09
$2\rightarrow2$	0.33	0.92	0.2
$2\rightarrow3$	4	0.9	1.45
$3\rightarrow1$	1.8	0.49	1.2
$3\rightarrow2$	1.1	0.49	0.78
$3\rightarrow3$	0.43	0.1	0.24

wave functions of this QCL for an applied field of 12.2 kV/cm and at 44 K are shown on the inset of Fig. 8. As in other studies, including ours,[10,11] it was supposed that the QCL is ideally periodic, i.e., consists in an infinite repetition of identical stages. This feature is taken into account in the determination of the energy levels and the corresponding wave functions. At first, the Schrödinger and Poisson equations are solved over the three stages. Then, by means of a proper shift in space and energy of the levels belonging to the central stage, we account for the periodicity of the QCL. Moreover, we assume periodic boundary conditions during the Monte Carlo, reinjecting in the central stage electrons that undergo interstage transitions.

The principle of operation of this QCL can be suitably described considering only five subbands, whose eigenenergies are labeled by e_λ in the following (see Fig. 8): Lasing occurs between levels 5 and 4, for a photon energy of $\Delta e_{54}=e_5-e_4=15$ meV. Levels 3 and 4 are resonantly coupled

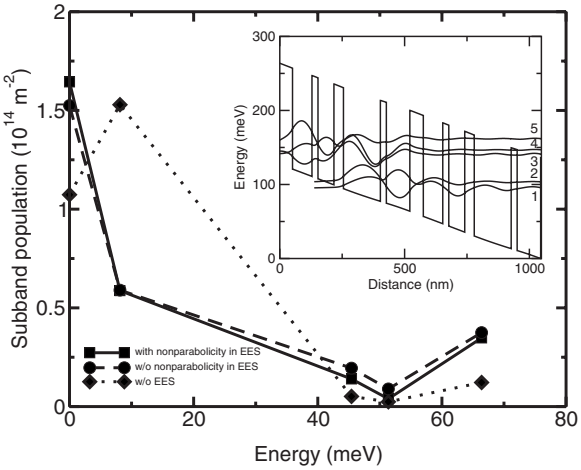

FIG. 8. The occupancy of different subbands with (solid line) and without (dashed line) accounting for the NP in the CCS interaction. The case without including EES in the simulation is also plotted in dotted line, closed diamond. Only discrete values, shown by the closed symbols, are meaningful. However, for readability these symbols have been connected by lines. The energy reference of all curves is the bottom of the first subband. Inset: Calculated potential profile and wave functions of the QCL in Ref. 27 obtained by a self-consistent resolution of Schrödinger and Poisson equations. The wave functions have been shifted in energy so that their respective zero corresponds to the quantized energy level. The temperature is 44 K, and the applied field is 12.2 kV/cm.

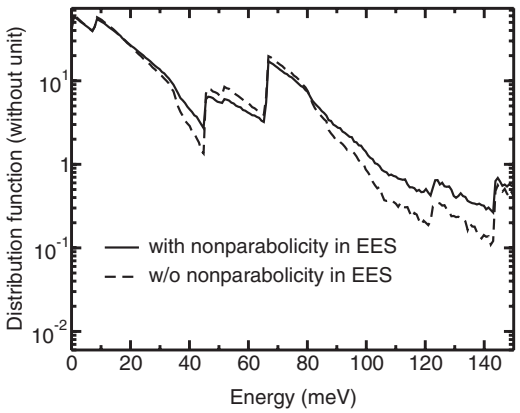

FIG. 9. Distribution function as a function of the energy for two EES models. Solid line: with NP in EES; Dashed line: without NP in EES. The energy reference of both curves is the bottom of the first subband.

and the energy separation $\Delta e_{32} \simeq 37$ meV almost matches the polar optic phonon energy (POP) of GaAs ($\sim$35 meV). Thus, the lower laser state, i.e., $\lambda=4$, is efficiently and selectively depopulated thanks to POP-emission scattering.

We now present the results of the Monte Carlo simulation of the structure of Ref. 27. We monitor 4000 electrons during 200 ps using a constant time step $\Delta t=2$ fs. The constant-energy contours were computed using an angle step of $\Delta\beta=2\pi/40$. With these parameters, when NP is accounted for in the simulation, the computational time is dramatically increased by a factor of about 10. The distributions of electron density among the different subbands with (solid line) and without (dashed line) accounting for the NP in the EES interaction are shown in Fig. 8. We have also plotted the electron population among the subbands without including the EES in the simulation (dotted line). One can observe that NP slightly alters the subband occupancy yielding a population inversion that is almost the same for the two EES models: whether NP is accounted for or not, the population inversion is 3×10^{13} m^{-2}.

This was expected from results of Fig. 4 since the NP coefficient of GaAs is low, and the energies encountered in QCL small. Thus, the high computational resources needed to account for NP in EES can be safely spared if "macroscopic quantities," such as population inversion, are examined. However, "microscopic quantities" may be altered by the EES model. To discuss this point and, more precisely, to better understand the influence of NP, the distribution function as a function of energy is represented in Fig. 9 with (solid line) and without (dashed line) accounting for the NP in the EES interaction. One can notice that accounting for NP in EES modifies the distribution function by warming the electrons: indeed, NP tends to set up Maxwellian distributions with higher electron temperatures. Table II summarizes the calculated subband temperatures obtained at the end of the simulation by the method described in Ref. 11. For almost all subbands, higher temperatures are obtained being the consequence of an increased number of EES events. Therefore, NP could strongly influence the electron dynamics and play a significant role if the frequency is reduced down to 1 THz.

TABLE II. Calculated subband temperatures T_λ (expressed in Kelvin) with and without including the NP in the EES.

	Without NP	With NP
T_1	127	157
T_2	125	146
T_3	93	113
T_4	60	45
T_5	94	121

IV. CONCLUSION

We have proposed a method for modeling CCS in semiconductors with nonparabolic bands by means of Monte Carlo simulation. The crucial point is the determination of the final states without the use of a systematic exploration of the **K** space. This is achieved in our algorithm by a formulation of the energy-conserving δ-function allowing the computation of the constant-energy contour in a numerically efficient way. This method is shown to correctly model equienergy lines in most usual cases, including highly nonparabolic conduction bands, e.g., in InAs, and warped valence bands in SiGe.

We have applied this Monte Carlo simulator to study the electron dynamics in an InAs heterostructure. To this aim, we investigated the relaxation of heated electrons initially located in an excited subband. It is shown that NP increases the carrier-carrier interaction, thus altering the transient regime. When a nonparabolic density of states is accounted for in the modeling of the carrier-carrier interaction, the electron relaxation is shown to be faster.

Then, the model has been used to address the validity of the parabolic approximation in a multisubbands QCL operating in the terahertz range. The influence of NP on population inversion is found to be small. Thus, for optimization purpose, the high CPU time required by a complete model of NP can be safely avoided. However, when internal quantities are investigated, such as subband temperatures, it is highly recommended to take the NP into account.

ACKNOWLEDGMENTS

The authors would like to thank the Institut de Développement et des Ressources en Informatique Scientifique (IDRIS) for generous allocation of computer time.

APPENDIX: CALCULATION OF $\Omega(\mathbf{W})$

In the following, we give the expression of the final density of states in the case of a Kane model for the electron effective mass.[18] Within this assumption, the dispersion relation is approximated by a second degree polynomial

$$\frac{\hbar^2\mathbf{K}^2}{2m_\lambda^*} = \varepsilon(1+\alpha_\lambda\varepsilon), \tag{A1}$$

where m_λ^* is the effective mass of subband λ and α_λ is the NP coefficient, both being averaged over the device length weighted by $|\varphi_\lambda(z)|^2$, the squared modulus of the wave function. In this case, $\Omega^{\mathrm{np}}(\mathbf{W})$ has the following expression:

$$\Omega^{\mathrm{np}}(\mathbf{W}) = \frac{2W}{\hbar^2}\left|\frac{2W^2+\mathbf{W}\cdot\mathbf{T}}{m^*_{\mu'}[1+2\alpha_{\mu'}\varepsilon_{\mu'}(\mathbf{W}+\mathbf{T}/2)]} + \frac{2W^2-\mathbf{W}\cdot\mathbf{T}}{m^*_{\lambda'}[1+2\alpha_{\lambda'}\varepsilon_{\lambda'}(\mathbf{W}-\mathbf{T}/2)]}\right|^{-1}. \quad \text{(A2)}$$

Note that with $\alpha \to 0$ and $m^*_{\lambda'} = m^*_{\mu'} \equiv m^*$, one recovers the limiting case of parabolic bands.

$$\Omega^{\mathrm{np}}(\mathbf{W}) \to \Omega^{\mathrm{parab}}(\mathbf{W}) = \frac{m^*}{2\hbar^2 W}. \quad \text{(A3)}$$

Reinjecting this result into Eq. (10), with the help of Eq. (3), one finds as expected the scattering rates expression in the case of parabolic bands [i.e., Eq. (9)] without using the factorization of the energy-conserving δ-function given by Eq. (7).

[1] W. H. Knox, C. Hirlimann, D. A. B. Miller, J. Shah, D. S. Chemla, and C. V. Shank, Phys. Rev. Lett. **56**, 1191 (1986).
[2] W. H. Knox, D. S. Chemla, G. Livescu, J. E. Cunningham, and J. E. Henry, Phys. Rev. Lett. **61**, 1290 (1988).
[3] K. W. Sun, T. S. Song, C.-K. Sun, J. C. Wang, M. G. Kane, S. Y. Wang, and C. P. Lee, Phys. Rev. B **61**, 15592 (2000).
[4] M. Hartig, S. Haackke, B. Deveaud, and L. Rota, Phys. Rev. B **54**, R14269 (1996).
[5] M. Hartig, S. Haackke, P. E. Selbmann, B. Deveaud, R. A. Taylor, and L. Rota, Phys. Rev. Lett. **80**, 1940 (1998).
[6] P. Harrison and R. W. Kelsall, Solid-State Electron. **42**, 1449 (1998).
[7] R. C. Iotti and F. Rossi, Appl. Phys. Lett. **76**, 2265 (2000).
[8] R. C. Iotti and F. Rossi, Appl. Phys. Lett. **78**, 2902 (2001).
[9] R. C. Iotti and F. Rossi, Phys. Rev. Lett. **87**, 146603 (2001).
[10] H. Callebaut, S. Kumar, B. S. Williams, Q. Hu, and J. L. Reno, Appl. Phys. Lett. **83**, 207 (2003).
[11] O. Bonno, J.-L. Thobel, and F. Dessenne, J. Appl. Phys. **97**, 043702 (2005).
[12] D. Pines and D. Bohm, Phys. Rev. **85**, 338 (1952).
[13] S. M. Goodnick and P. Lugli, Phys. Rev. B **37**, 2578 (1988).
[14] L. Rota, P. Lugli, T. Elsaesser, and J. Shah, Phys. Rev. B **47**, 4226 (1993).
[15] M. Moško, A. Mošková, and V. Cambel, Phys. Rev. B **51**, 16860 (1995).
[16] K. Kalna, M. Moško, and F. M. Peeters, Appl. Phys. Lett. **68**, 117 (1996).
[17] K. Kalna and M. Moško, Phys. Rev. B **54**, 17730 (1996).
[18] J.-L. Thobel, O. Bonno, F. Dessenne, and H. Boutry, J. Appl. Phys. **92**, 5286 (2002).
[19] M. V. Fischetti and S. E. Laux, Phys. Rev. B **38**, 9721 (1988).
[20] A. Abramo, R. Brunetti, C. Jacoboni, F. Venturi, and E. Sangiorgi, J. Appl. Phys. **76**, 5786 (1994).
[21] M. V. Fischetti, S. E. Laux, and E. Crabbé, J. Appl. Phys. **78**, 1058 (1995).
[22] M. V. Fischetti and S. E. Laux, J. Appl. Phys. **89**, 1205 (2001).
[23] R. C. Iotti and F. Rossi, Semicond. Sci. Technol. **19**, 323 (2004).
[24] E. O. Kane, Phys. Rev. **159**, 624 (1967).
[25] D. Harrison, R. A. Abram, and S. Brand, J. Appl. Phys. **85**, 8178 (1999).
[26] G. Gilat and L. J. Raubenheimer, Phys. Rev. **144**, 390 (1966).
[27] B. Williams, H. Callebaut, S. Kumar, Q. Hu, and J. Reno, Appl. Phys. Lett. **82**, 1015 (2003).
[28] M. A. Osman and D. K. Ferry, Phys. Rev. B **36**, 6018 (1987).
[29] O. Bonno, J.-L. Thobel, and F. Dessenne, J. Comput. Electron. **5**, 103 (2006).
[30] P. Harrison, *Quantum Wells, Wires, and Dots: Theoretical and Computational Physics* (Wiley, Chichester, 2000).
[31] O. Bonno, J.-L. Thobel, and F. Dessenne, Physica E (Amsterdam) **33**, 13 (2006).
[32] M. Moško and A. Mošková, Phys. Rev. B **44**, 10794 (1991).
[33] C. Jacoboni and L. Reggiani, Rev. Mod. Phys. **55**, 645 (1983).
[34] O. Madelung, *Semiconductor Basic Data* (Springer, Berlin, 1996).
[35] S. Rodriguez-Bolivar, F. M. Gomez-Campos, F. Gamiz, and J. E. Carceller, J. Appl. Phys. **97**, 013702 (2005).
[36] E. O. Kane, J. Phys. Chem. Solids **1**, 82 (1956).
[37] F. L. Madarasz, J. E. Land, and P. M. Hemeger, J. Appl. Phys. **52**, 4646 (1981).
[38] J.-L. Thobel, L. Baudry, P. Bourel, F. Dessenne, and M. Charef, J. Appl. Phys. **74**, 6274 (1993).
[39] P. Borowik and J.-L. Thobel, J. Appl. Phys. **84**, 3706 (1998).
[40] A. Tomita, J. Shah, J. E. Cunningham, S. M. Goodnick, P. Lugli, and S. L. Chuang, Phys. Rev. B **48**, 5708 (1993).
[41] L. Rota, F. Rossi, P. Lugli, and E. Molinari, Phys. Rev. B **52**, 5183 (1995).
[42] H. Callebaut and Q. Hu, J. Appl. Phys. **98**, 104505 (2005).
[43] J. Mc Tavish, D. Indjin, and P. Harrison, J. Appl. Phys. **99**, 114505 (2006).
[44] V. D. Jovanovic, S. Hofling, D. Indjin, N. Vukmirovic, Z. Ikonic, P. Harrison, J. P. Reithmaier, and A. Forchel, J. Appl. Phys. **99**, 103106 (2006).
[45] C. Jirauschek, G. Scarpa, P. Lugli, M. S. Vitiello, and G. Scamarcio, J. Appl. Phys. **101**, 086109 (2007).
[46] E. Bellotti, K. Driscoll, T. D. Moustakas, and R. Paiella, Appl. Phys. Lett. **92**, 101112 (2008).